NUMERICAL ANALYSIS OF FLOW STRUCTURE AND ENERGY LOSS IN AN IMPELLER SIDE CHAMBER OF A MOLTEN SALT PUMP

by

Yong-Xin JIN[a], De-Sheng ZHANG[a,*], Rui-Jie ZHAO[a], Lei SHI[a], and Wei-Dong SHI[a,b]

[a] Research Center of Fluid Machinery Engineering and Technology, Jiangsu University, Zhenjiang, Jiangsu, China
[b] School of Mechanical Engineering, Nantong University, Nantong, Jiangsu, China

Original scientific paper
https://doi.org/10.2298/TSCI1904333J

The internal flow structure and the energy loss in the first stage impeller side chamber of a molten salt pump for solar thermal power generation were investigated numerically. The flow field in the model pump was simulated based on the RANS equation using the standard k-ε turbulence model. The results indicate that the rotating speed of core flow in the front impeller side chamber is higher than the tangential velocity at the maximal radius of the front shroud. However, the core flow in the rear impeller side chamber gives an opposite trend. Meanwhile, the radial velocity at the boundary-layer separation point on the front impeller side chamber stationary wall decreases initially and then increases with the radius while it only decreases in the rear impeller side chamber. For the energy loss, the percentage of the disk friction loss to total energy consumption reduces as the flow rate increases, while the absolute value of disk friction loss on the front shroud keeps almost constant and the loss on the rear shroud decreases with the increasing flow rate.

Key words: *molten salt pump, impeller side chamber, energy loss, flow structure*

Introduction

Molten salt is used in the new generation of nuclear and solar thermal power systems as a good heat transfer medium, and the molten salt pump (MSP) is of great importance in transferring high temperature molten salt and is widely used in energy facilities [1, 2]. In high temperature condition, the axial thermal deformations of pump's rotary and static parts are different, causing a mismatch between the rotor and the stator. For this reason, the front and back rings are extended, which makes the impeller side chamber structure different from common pumps.

In common semi-open impeller, the increase in the clearance of front shroud can reduce the heat and change the load of blade [3]. The flow and pressure in clearance are changed [4, 5]. In addition, the disk friction loss (DFL) in impeller side chamber is mainly due to fluid viscosity and occurs mainly in the turbulent boundary-layer [6].

The impeller side chamber structure, clearance leakage and fluid viscosity have a great influence on the flow pattern in the impeller side chamber, so the flow field in impeller side chamber was studied for different specific speeds, the model of accurately predicting the DFL and the flow field distribution were obtained in [7, 8].

* Corresponding author, e-mail: zds@ujs.edu.cn

Daily *et al.* [9] simplified the liquid flow in the impeller side chamber to a rotating motion around the fixed axis in the enclosed chamber. Then a 3-layer flow mathematical model of the liquid motion in pump chamber was established based on the experimental results. Senoo *et al.* [10] thought that the 3-layer flow model had neglected the existence of radial flow in impeller side chamber, and proposed a 4-layer flow mathematical model. Therefore, Li *et al.* [11] and Yang *et al.* [12] validated the 4-layer flow model by considering the axial clearance of the pump cavity and Reynolds number, and the results were in good agreement with the experimental data.

Besides the aforementioned studies, investigations on MSP mainly focused on hydraulic performance, sealing structure and structural characteristics [13]. In this paper, the numerically analytical method will be used to investigate the flow structure and energy loss in the special impeller side chamber under different operating conditions.

Physical model and numerical set-up

Physical model

The three-stage model pump with guide vanes has a long axis, and the basic geometrical parameters at design point are: H = 150 m, Q_d = 350 m^3/h, n = 1450 rpm. A large impeller side chamber clearance is set to ensure that the impeller shroud and the guide vane component cannot interfere each other, and the details are presented in fig.1. The whole flow field will be simulated and the modeling domain is the first stage impeller side chamber. The numerical results are compared with the experiments in order to verify the accuracy of the simulation.

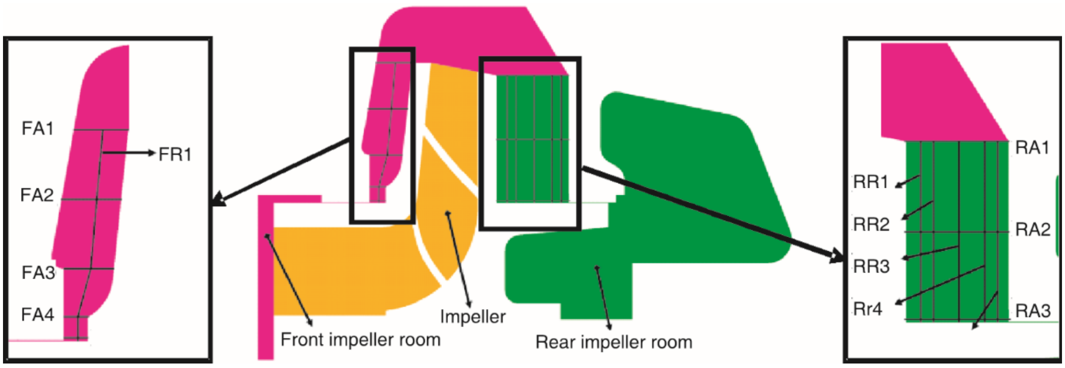

Figure 1. Calculation domain

Grid independence and turbulence model

The whole flow field calculation was based on the RANS equation and standard k-ε turbulence model.

It is commonly known that excessive grids will cost too much computing resource and time, so an appropriate number of grid nodes is necessary. Three structured mesh with high quality are used to check the grid independence, as shown in fig. 2. The calculation results under rated condition are shown in tab. 1 and the grid nodes of $2.52 \cdot 10^7$ was selected finally.

Numerical set-up

For consistency, the medium in both experiment and calculation is water. The calculated domain corresponding to rotating components were set as rotation domain. The interface between rotor and stator were set as *frozen rotor*. All physical surfaces were set as non-slip walls. The classical boundary conditions were established: mass-flow rate was imposed at the inlet section and total pressure was assigned at the opening outlet, which was shown in fig. 3.

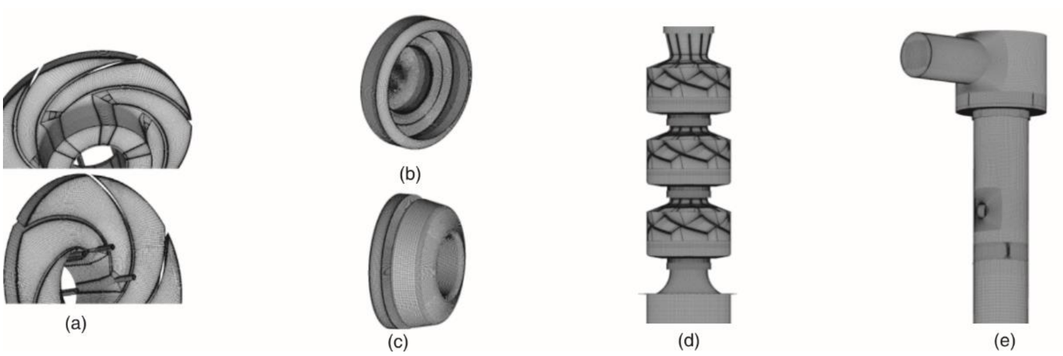

Figure 2. Structured grids for the calculated domain; (a) impeller, (b) front impeller room, (c) rear impeller room, (d) suction stage, and (e) discharge chasing

Results and discussion

Hydraulic performance

The whole flow field calculation was performed under five flow rate conditions ($0.4Q_d$, $0.6Q_d$, $0.8Q_d$, $1.0Q_d$, $1.1Q_d$, and Q_d are the design point flow rates, respectively). The comparison between numerical and experimental data, including the head and efficiency of the model pump, is illustrated in fig. 4. The discrepancy of the head and efficiency is proximately 2.4% and 4.43% under all conditions, and the maximum error occurs under the small flow rate conditions because of the chaotic flow field. The results indicate that the numerical data is reliable and can be accepted in present study.

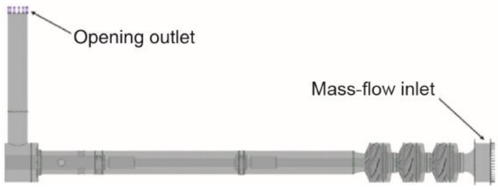

Figure 3. Calculation domain and boundary conditions

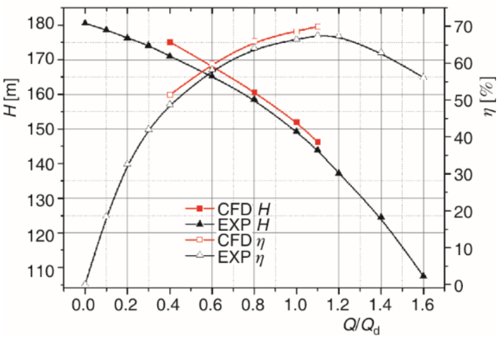

Figure 4. Numerical and experimental result

Tangential velocity profiles in impeller side chamber

In the following figures, figs. 5 and 6, l/L is the relative axial length position, V_u/U represents the dimensionless tangential velocity, where l is the distance from shroud, and L is the width of the section. The V_u is the tangential velocity and U is the wall rotating speed corresponding to the radius section.

Distribution of tangential velocity: In the front of the impeller side chamber, the tangential velocity is close to the front shroud rotation speed as radius decreases. The distribution of the front impeller side chamber tangential velocity indicates that the larger the radius is, the greater the shear stress and the velocity gradient on the impeller front shroud are, fig. 5.

In general, the tangential velocity on different sections shows a tendency to rise as the flow rate increases. Furthermore, the tangential velocity on RA1 Section near the impeller outlet is relatively large, fig. 6. When the distance from the impeller exit increases, the fluctuation amplitude of tangential velocity on RA2 and RA3 Sections becomes smaller than that on the RA1 Section. In particular, there is a sudden change of the tangential velocity on RA1 Section close to rear shroud, and this phenomenon is in agreement with the model proposed in [11, 12].

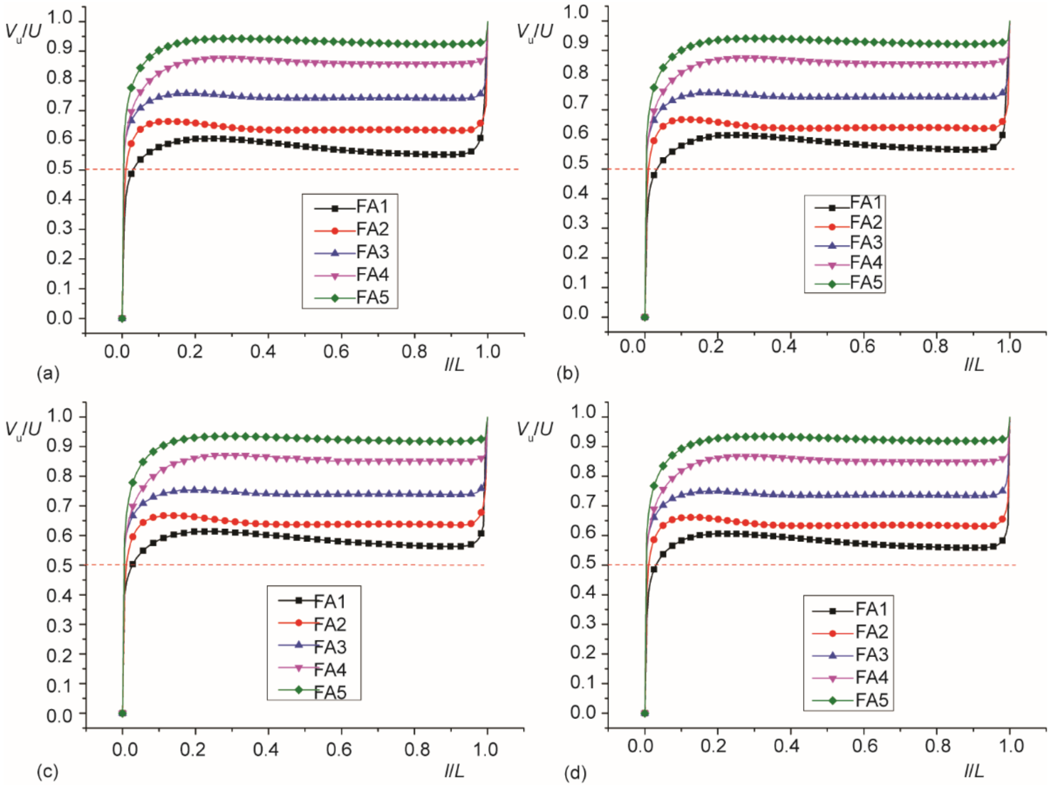

Figure 5. Distribution of tangential velocity in front impeller side chamber; (a) 0.6 Q_d, (b) 0.8 Q_d, (c) 1.0 Q_d, and (d) 1.1 Q_d

Distribution of tangential velocity: The tangential velocity on FR1 is shown as a V-type structure and presented in fig. 7. The main reason for the special tangential velocity distribution is the viscous friction. The front shroud wall consists of radial wall and axial wall, and the two walls act on the fluid in the front impeller side chamber. In the middle position of the radius, the distance of shroud and wall changes and then gives rise to the tangential velocity to reduce to its minimum. Then radius continues to increase and the clearance width has only slide change, while the tangential velocity keeps increase. All previously presented is shown in fig. 7, and the results are support by [8].

The radial distribution of the tangential velocity in rear impeller side chamber changes greatly, fig. 8. Under the simulated working conditions, the magnitude of tangential velocity is in the range from 0.38 to 0.54, and it increases with the flow rate. The distribution of tangential velocity in the gap between the front shroud and rear impeller side chamber is consistent with the conclusion in [7].

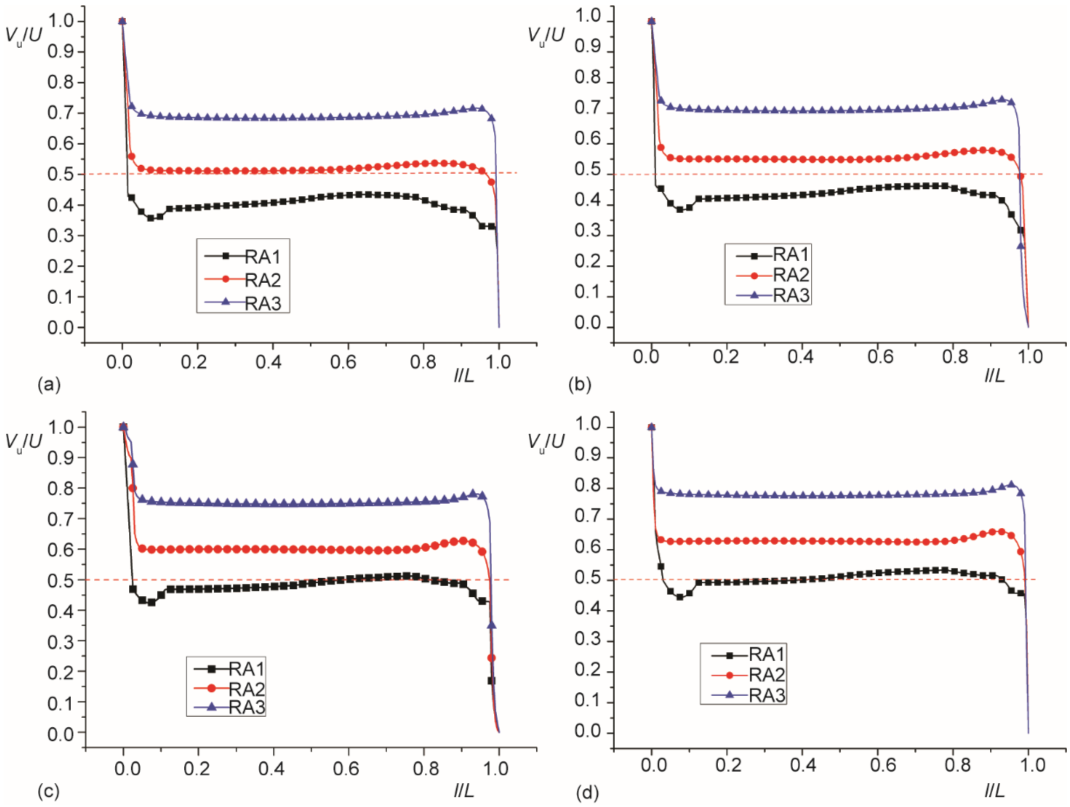

Figure 6. Distribution of tangential velocity in rear impeller side chamber; (a) 0.6 Q_d, (b) 0.8 Q_d, (c) 1.0 Q_d, and (d) 1.1 Q_d

Radial velocity profiles in impeller side chamber

The distribution of radial velocity in axial direction in front impeller side chamber is shown in fig. 9. Due to the centrifugal force on front shroud rotating wall, the positive radial velocity of boundary layer separation increases with the increase of radius. Before the boundary layer separation, the magnitude of negative radial velocity on stator is reduced initially and then increases as the axial coefficient l/L increases, but the negative radial velocity at section FA5 has the maximal value both for four working conditions. On FA1 section, the negative radial velocity is at l/L = 0~0.3 and the radial velocity is positive from 0.3 to 1.0. Then, both the FA2 and FA3 sections have a transition of radial velocity at l/L = 0.2, but it is almost at l/L = 0.4 for FA4 and FA5 sections.

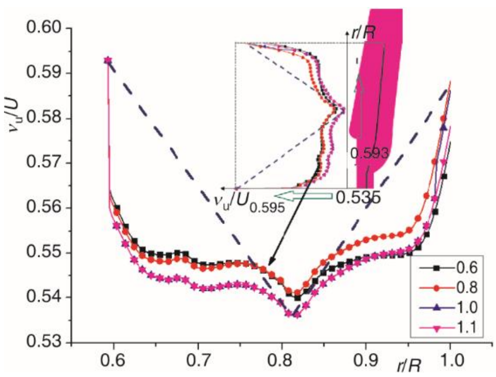

Figure 7. Distribution of tangential velocity in impeller front shroud

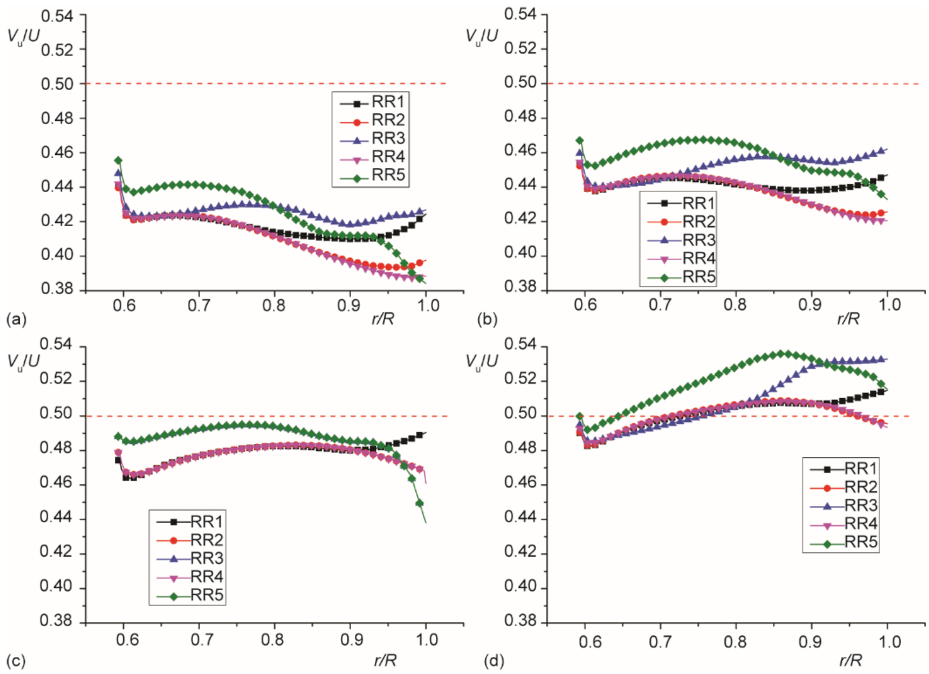

Figure 8. Distribution of tangential velocity in rear impeller side chamber; (a) 0.6 Q_d, (b) 0.8 Q_d, (c) 1.0 Q_d, and (d) 1.1 Q_d

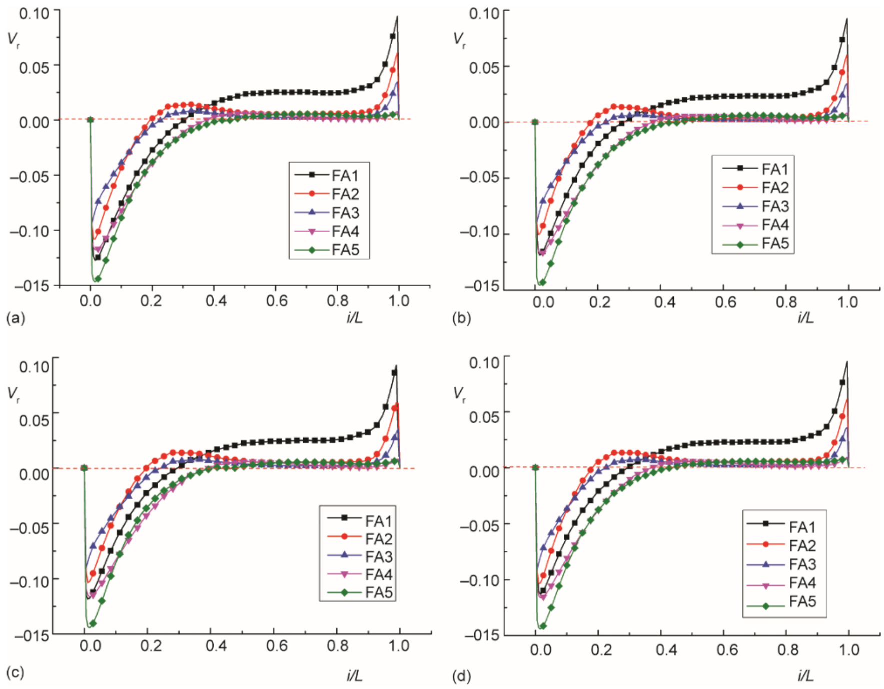

Figure 9. Distribution of radial velocity in front impeller side chamber; (a) 0.6 Q_d, (b) 0.8 Q_d, (c) 1.0 Q_d, and (d) 1.1 Q_d

According to fig. 10 in which the distribution of radial velocity in axial direction in impeller rear impeller side chamber is displayed, it concludes that the transitional velocity (shown by the dash line) on rear shroud increases with the radius, but it is opposite on the stator. On RA1 section, the radial velocity is positive in the range of 0~0.7 and it has negative magnitude at l/L = 0.7~1.0. Additionally, section RA3 has a transitional radial velocity more close to l/L = 1.0 compared with section RA2.

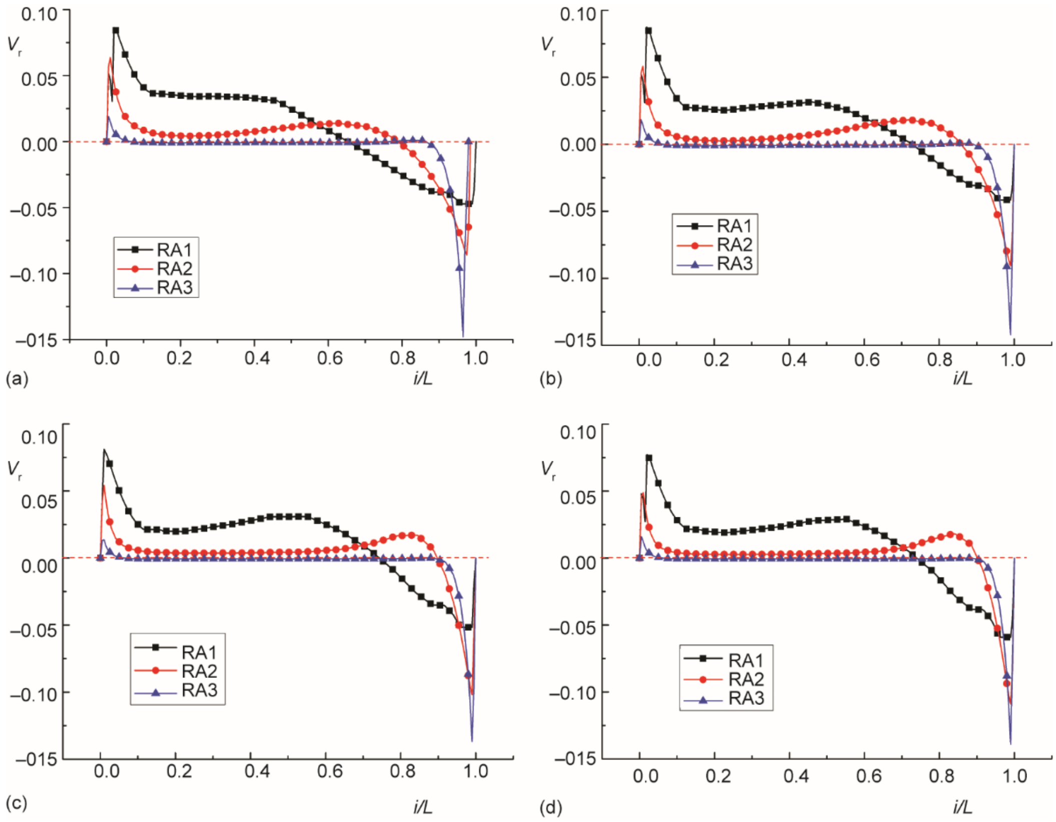

Figure 10. Distribution of radial velocity in rear impeller side chamber; (a) 0.6 Q_d, (b) 0.8 Q_d, (c) 1.0 Q_d, and (d) 1.1 Q_d

Energy loss in impeller side chamber

Due to the viscosity of the fluid, the front and rear shrouds of the impeller will lead the fluid to rotating in the course of rotation accompanied with a centrifugal movement. The process of the fluid motion on the wall boundary of the impeller shroud is essentially the process of energy transfer from the impeller shroud wall to flow, and the energy loss will be inevitably accompanied with the energy transport. Because of the variable geometries of the front and rear impeller side chamber, the flow characteristics of the fluid in impeller side chamber is different, and the energy loss is changed which is induced by the impeller side chamber with different geometries and the working conditions.

As shown in fig. 11, the percentage of DFL to total energy consumption and energy loss reduces with the increase of the flow rate, and the percentage of loss energy decreases obviously. The percentage of energy loss by the rear shroud to energy consumption and total energy loss are higher than that by the front shroud. As the flow rate increases, the absolute loss of the front shroud does not change clearly, but the rear shroud has a certain decline of absolute loss. The volume of front impeller side chamber is only half of the rear impeller side chamber, resulting in the energy of rotating core flow in impeller side chamber being generated from the friction between the fluids and shroud wall, which causes the rear shroud energy loss to be higher than that of front shroud.

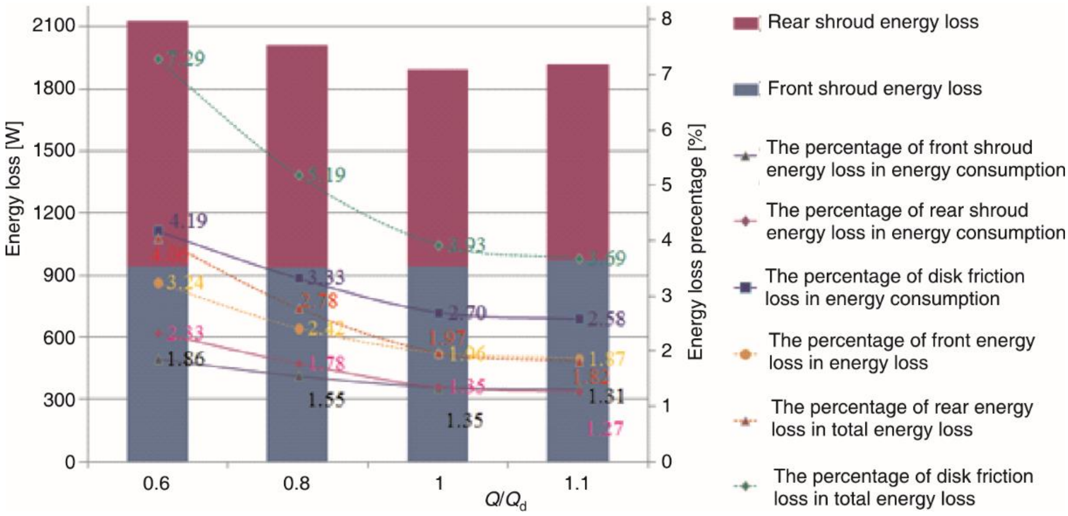

Figure 11. Energy loss mapping (*for color image see journal web site*)

Conclusion

The significant conclusions can be drawn as follows.

- Under 0.6 Q_d, 0.8 Q_d, 1.0 Q_d, and 1.1 Q_d operating conditions, respectively, the tangential velocity is almost constant. The radial distribution of the tangential velocity in front impeller side chamber presents a V-type structure and it is not influenced by the flow rate obviously.
- The distribution of tangential velocity in rear impeller side chamber is similar to that in front impeller side chamber. The tangential velocity near the impeller outlet is relatively large and the radial distribution of tangential velocity in rear impeller side chamber varies considerably with the increasing flow rate. Additionally, the critical velocity on rear shroud increases as the radius increases, but this is contrary on the stator wall.
- The percentage of DFL to energy consumption and total energy loss reduces with the increase of the flow rate. However, the absolute value of DFL by front shroud or in the clearance between the front shroud and shell is almost constant and the loss on rear shroud decreases with the increase of the flow rate.

Acknowledgment

This work is supported by the Key Research and Development Plan Foundation of Jiangsu Province (Grant No. BE2015146), Scientific and Technological Achievements Translate Foundation of Jiangsu Province (Grant No. BA20116167), Innovation Project for Postgraduates of Jiangsu Province (Grant No. KYCX17_1772), 333Project of Jiangsu Province

(Grant No. 2016III-2731), Six Talent Peaks Project in Jiangsu Province (Grant No. HYGC-008) and Qing Lan Project.

References

[1] Garbrecht, O., *et al.*, CFD-Simulation of a New Receiver Design for a Molten Salt Solar Power Tower, *Solar Energy*, *90* (2013), 2, pp. 94-106
[2] Ortega, J., *et al.*, Central Receiver System Solar Power Plant Using Molten Salt as Heat Transfer Fluid, *Journal of Solar Energy Engineering*, *130* (2008), 2, pp. 247-266
[3] Ayad, A. F., *et al.*, Effect of Semi-Open Impeller Side Clearance on the Centrifugal Pump Performance Using CFD, *Aerospace Science & Technology*, *47* (2015), Dec., pp. 247-255
[4] Will, B. C., *et al.*, Investigation of the Flow in the Impeller Side Clearances of a Centrifugal Pump with Volute Casing, *Journal of Thermal Science*, *21* (2012), 3, pp. 197-208
[5] Piesche, D. I., *et al.*, Investigation of the Flow in the Impeller-Side Space of Rotary Pumps with Superimposed Throughflow for the Determination of Axial Force and Frictional Torque, *Acta Mechanica*, *78* (1989), 3, pp. 175-189
[6] Wang, X. Y., *et al.*, Numerical Study of Flow Characteristics in the Impeller Side Chamber of Centrifugal Pump, *Transactions of the Chinese Society for Agricultural Machinery*, *40* (2009), 4, pp. 86-90
[7] Liu, H. L., *et al.*, Calculation of Disk Friction Loss of Centrifugal Pumps, *Transactions of the Chinese Society of Agricultural Engineering*, *22* (2006), 12, pp. 107-109
[8] Guelich, J. F., *Centrifugal Pumps*, Springer-Verlag, Berlin, Germany, 2014
[9] Daily, J. W., *et al.*, Chamber Dimension Effects on Induced Flow and Frictional Resistance of Enclosed Rotating Disks, *Journal of Basic Engineering*, *82* (1960), 1, pp. 217
[10] Senoo, Y., *et al.*, An Analysis on the Flow in a Casing Induced by a Rotating Disk Using a Four-Layer Flow Model, *Transactions of the Japan Society of Mechanical Engineers*, *98* (1976), 2, pp. 2462-2471
[11] Li, W., *et al.*, Experimental Study of the New Method on Reducing Friction Losses of Disk, *Journal of Hydrodynamics*, *13* (1998), 1, pp. 65-70
[12] Yang, J. H., *et al.*, Mathematical Model of Flow inside a Centrifugal Pump Casing, *Transactions of the Chinese Society of Agricultural Machinery*, *34* (2003), 6, pp. 68-72
[13] Shao, C. L., *et al.*, Experimental Investigation of the Full Flow Field in a Molten Salt Pump by Particle Image Velocimetry, *Journal of Fluids Engineering*, *137* (2015), 10, ID 104501

Paper submitted: December 21, 2017
Paper revised: June 18, 2018
Paper accepted: June 18, 2018